UCRL-JC-152386

Direct Observation of a Nonlocal Heat Wave

G. Gregori, H. Glenzer, J. Knight, C. Niemann, D. Price, D. H. Froula, M. J. Edwards, R. P. J. Town, A. Brantov, W. Rozmus, V. Yu Bychenkov

August 18, 2003

Physical Review Letters

This document was prepared as an account of work sponsored by an agency of the United States Government. Neither the United States Government nor the University of California nor any of their employees, makes any warranty, express or implied, or assumes any legal liability or responsibility for the accuracy, completeness, or usefulness of any information, apparatus, product, or process disclosed, or represents that its use would not infringe privately owned rights. Reference herein to any specific commercial product, process, or service by trade name, trademark, manufacturer, or otherwise, does not necessarily constitute or imply its endorsement, recommendation, or favoring by the United States Government or the University of California. The views and opinions of authors expressed herein do not necessarily state or reflect those of the United States Government or the University of California, and shall not be used for advertising or product endorsement purposes.

Direct observation of a nonlocal heat wave

G. Gregori,* S. H. Glenzer,* J. Knight,* C. Niemann,* D. Price,* D. H. Froula,* M.
J. Edwards,* R. P. J. Town,* A. Brantov,† V. Yu. Bychenkov,‡ and W. Rozmus†

(Dated: August 18, 2003)

We present the first observation of a nonlocal heat wave by measuring spatially and temporally resolved electron temperature and electron density profiles in a laser produced nitrogen plasma. Absolutely calibrated measurements have been performed by resolving the ion-acoustic wave spectra across the plasma volume with Thomson scattering. We find that the experimental electron temperature and electron density profiles disagree with flux-limited models, but are consistent with transport models that account for the nonlocal effects in heat conduction by fast electrons.

Nonlocal heat transport is a fundamental process for the laser plasma interaction in inertial confinement fusion (ICF) experiments, as well as for the correct design of ICF ignition targets [1]. Controlled energy deposition by intense lasers into a radiation cavity (hohlraum) must be properly modelled to achieve the desired symmetric convergence of implosion ICF capsules. Key issues that need to be addressed are the degree of heat transport inhibition by both nonlocal electrons and magnetic fields [2, 3] together with a validation of the predictive capability of plasma conditions in gas filled hohlraums [4]. Since the early experiment of Gray and Kilkenny [5] and Fokker-Planck simulations [6–8] which first provided evidence of heat flux inhibition and nonlocal transport, a large theoretical effort [9–13] has been aimed to identify and model the correct mechanism for heat transport in laser produced plasmas. In plasmas with small temperature gradients, the heat transport is described by the classical Spitzer-Härm theory [14]. This is valid when $\lambda_{ei} \lesssim 0.01 L_t$, where λ_{ei} is the electron-ion mean free path and L_t is the spatial scale for the thermal gradients. In laser irradiated plasmas, however, the intense localized heating at the beam focus drives an expanding heat wave with steep temperature gradients. As a result, the energy flux described by the local Spitzer-Härm theory becomes invalid as the fast heat carrying electrons broaden the heat front. In addition, strong heat flow in laser plasmas can drive ion acoustic wave instability by the return current of slow electrons [15, 17]. Enhanced ion acoustic fluctuations reduce further electron heat conductivity and increase laser light absorption [16] above the collisional inverse bremsstrahlung rate.

In this letter, we report the first observation of nonlocal heat wave propagation. We have experimentally obtained spatially and temporally resolved electron temperature and density profiles of the heat wave evolution and used them to test radiation-hydrodynamics, Fokker-Planck, and reduced nonlinear, nonlocal transport modeling. Direct comparison showed that the late time evolution of the heat wave is well reproduced by Fokker-Planck simulations and by the nonlinear nonlocal reduced model, but it is not in agreement with radiation-hydrodynamics predictions.

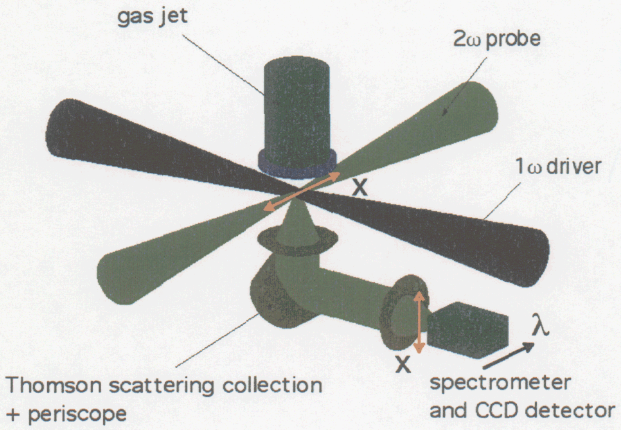

FIG. 1: (color) Experiment setup for Thomson scattering imaging. The temperature and density profiles are obtained across the (1ω) driver beam. Two additional mirrors (periscope) used to flip the image are not shown in the figure.

The experiments have been performed at the *Janus* laser facility at the Lawrence Livermore National Laboratory. The setup is illustrated in Figure 1. We produce the plasma by heating a ∼2 mm diameter nitrogen gas jet operating at 4.8 MPa upstream pressure with a Gaussian 1.4 ns FWHM, ∼100 J driver beam at the fundamental frequency of 1064 nm (1ω). The plasma is then probed perpendicularly to the driver beam with a 130 ps, 0.2 J beam operating at 532 nm (2ω). The probe beam was then imaged, on a gated charge-coupled device (CCD) camera, along a 100 μm wide slit of a 0.67 m, 1200 grooves/mm spectrometer used in second order. The imaging optics were placed at 90° to the plane formed by the driver and the probe beams. In order to examine the heating of the plasma, the probe beam was fired at various times during the driver beam pulse. Electron temperature profiles can be extracted from the Thomson scattering signal based on the wavelength separation of the ion acoustic waves. The electron density is obtained self-consistently from absolute intensity Rayleigh scattering calibration of the instrument response [18] via

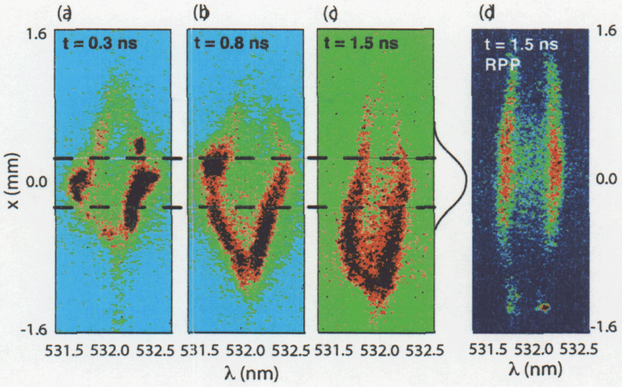

FIG. 2: (color) Spatially resolved Thomson scattering spectra. The horizontal axis is wavelength, centered at 532 nm, and the vertical axis is space along the probe beam. The probe beam propagates from the bottom to the top. Panels (a) to (c) refer to TS signals using an unsmoothed Gaussian (1ω) driver beam, with the dashed lines indicating the area of heating. Panel (d) refers to TS from a RPP driver beam. Shot-to-shot accuracy in the location of $x = 0$ is $\sim$150 μm.

the following relation:

$$S(k)n_e = n_R \frac{\sigma_R}{\sigma_{Th}} \frac{P_{Th} I_R}{P_R I_{Th}}, \tag{1}$$

where $S(k)$ is the frequency-integrated spectral density function (or static form factor), n_e is the electron density, n_R is the density of the gas used in the Rayleigh calibration, P_{Th} and P_R are the total Thomson and Rayleigh scattered intensities, respectively, into the CCD detector, and I_{Th} and I_R are the total incident laser intensities in the Thomson and Rayleigh scattering experiments, respectively. The ratio of the Thomson cross section to the Rayleigh cross section σ_R/σ_{Th} is well known for nitrogen [19]. The driver and probe beams spot size were also measured with Rayleigh scattering by imaging the entire beams on the CCD camera and by using the spectrometer in zero*th* order with the entrance slit fully open. The driver beam spot at target chamber center was measured to be $\sim$320 μm, while the probe beam was $\sim$120 μm in diameter. The time resolution is determined by the probe pulse length to be 130 ps. Timing errors were estimated from the laser trigger jitter to be on the order of 150-200 ps. Spatial resolution, instead, is in the order of $\sim$50 μm.

Figure 2 shows Thomson scattering (TS) spectra for three different times during the heating of a plasma. We have inferred temperature gradients from the spatially varying separation of the two ion-acoustic features. The gradients are steeper at the beginning of the pulse and moderate at the end of the laser pulse. In order to test the uniformity of the gas jet prior to the driver heating, we have illuminated the jet with a smoothed driver beam. Using a 1ω random phase plate (RPP) with $\sim$2 mm spot-size we checked that the ion-acoustic features remain parallel and constant in intensity over the entire scattering volume, indicating homogenous gas jet conditions. The temperature profile has been extracted by fitting the whole profile with the frequency-dependent TS form factor $S(k,\omega)$ [20]. Since the separation between the ion-acoustic features is also a function of electron density and ionization state, the electron density needs to be determined self-consistently from the Rayleigh scattering calibration. In addition, the ionization state, Z, is calculated using an atom-averaged Thomas-Fermi model [21], giving Z in the range 4-7 for T_e in the range 20-350 eV. This procedure allows a direct correlation between the separation of the TS peaks and the electron temperature. Including errors in the determination of Z, the measured absolute temperature data are thus determined with an accuracy of 20%; and the relative T_e profiles to 10% accuracy.

In contrast to the case of a RPP driver beam (Fig. 2d), where the scattered intensity remains almost constant across the heated plasma region, in the absence of smoothing, there is an asymmetry in the Fig. 2a-c intensity profiles from bottom to top at the later times. We have found that the unsmoothed high intensity pump can drive the filamentation instability with an amplitude gain length comparable to be beam waist [22]. When the probe beam crosses the region heated by the pump, it undergoes multiple scattering on large-amplitude long-wavelength density fluctuations produced by the filamentation instability of the pump beam. Such density fluctuations can randomize the probe beam over distances of the order of few hundred microns (cf Ref. [23]), and the resultant plasma induced smoothing of the Thomson probe thus reduces its intensity by spreading the beam and could account for the lower scattering signal in the top part of Fig. 2b-c. On the other hand, left-to-right asymmetry in the TS spectra is related to the presence of hot-spots in the unsmoothed pump intensity distribution, which drive asymmetric transverse temperature gradients. In the analysis reported in this paper the profiles have been obtained from the lower half of the TS images. Clearly, this introduces an overall uncertainty in the absolute electron density values by a factor $\sim$2. The measured relative density profiles are determined with 20% accuracy.

Figures 3 and 4 show the electron temperature and electron density profiles for the focused driver beam, at different times during the heating cycle. The electron mean free path, using the measured values of electron temperature and density at the center of the profile ($T_e \simeq 300$ eV, $n_e \simeq 10^{19}$ cm^{-3}) is $\lambda_{ei} \sim 30\mu$m, comparable with the temperature gradient scale-length from Figure 3 along together with numerical simulations. Under these conditions, nonlocal transport is expected to play an important role. In addition, we observe a *nonlocal* heat wave which propagates into the plasma far beyond

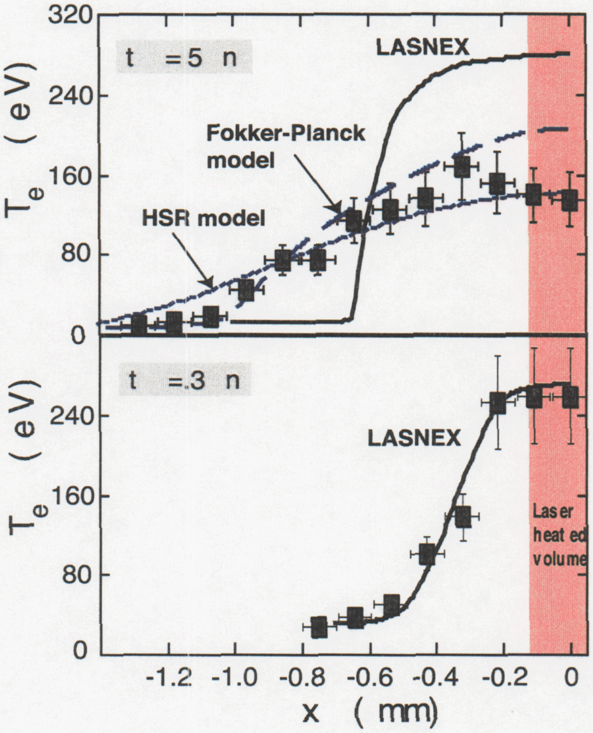

FIG. 3: (color) Electron temperature profiles at $t = 0.3$ ns and $t = 1.5$ ns. The shaded area corresponds to the heated area by the 1ω driver beam.

the predicted distance by flux-limited models.

The nonlocal behavior is evident from the comparison of the experimental temperature profiles with the LASNEX code [24], a multigroup, flux-limited, non-LTE (local thermodynamic equilibrium) diffusion code, which is widely used in the design of fusion targets for ICF. In fluid codes such as LASNEX, the usual approach is to model the relation due to nonlocal heat flow by a local law [25] $\mathbf{q} = \min(f\mathbf{q}_{fs}, \mathbf{q}_{SH})$, where $\mathbf{q}_{fs}$ is the free-streaming flux, $\mathbf{q}_{SH}$ is the classical heat flow, and f is a flux-limiter factor. Given the measured temporal and spatial intensity profiles of the driver beam, the problem has been solved in cylindrical geometry. Starting from a uniform gas density, and assuming a flux-limited factor $f = 0.05$, calculated T_e and n_e profiles are obtained at various time intervals.

At the beginning of the heater pulse ($t = 0.3$ ns), LASNEX calculations agree well with the experimental temperature profiles. At these early times, the heat wave is directly correlated to the driver beam profile, that was measured with the spatially resolved Rayleigh scattering images of the 1ω beam. At later times, however, weakly collisional fast electrons carry heat far away from the heated central region. As seen in Figure 3, at $t = 1.5$ ns, the measured heat front position exceed the LASNEX prediction by a factor ~2, resulting in a temperature profile which is not as steep as expected from a local theory.

We find that density profiles also reflect the propagation mechanism of the heat wave. Figure 4 shows LASNEX simulations together with measured electron density profiles at two different times. As the driver beam deposits heat in the central region of the plasma, the increased thermal pressure pushes electrons away and they bunch at the heat front. LASNEX predicts the initial stage of the hydrodynamic expansion with the steepening of the density wave up to $t \lesssim 0.5$ ns. However, at the end of the heater pulse, we see a narrow spike in the electron density profile calculated by LASNEX at a position corresponding to the front of the heat wave. Such an effect is not consistent with the measured profiles, which show flat profiles extending over a wider region. Again, we interpret this as a consequence of nonlocal heat transport which results in limited local fluxes with a redistribution of the heat over a larger spatial region.

We have also performed full nonlocal calculations using SPARK [26, 27], a 2D code which solves the Fokker-Planck equations in the diffusion approximation. In these calculations the numerical grid was set up in a cylindrical geometry similarly to LASNEX. In the numerical setup, laser absorption via inverse bremsstrahlung was modified in order to obtain the same initial T_e conditions as in LASNEX.

At $t = 1.5$ ns, we see from the temperature plot of Figure 3 that SPARK reproduces well the measured profile, even far from the central region of the plasma. In contrast to the LASNEX result, SPARK density profile is flat over the entire region in agreement with the measured one, but slightly offset to higher values far from the central heated region. These differences may be explained by the fact that SPARK does not use a self-consistent equation of state to calculate the degree of ionization of the plasma (in the SPARK calculations we have assumed $Z = 7$ throughout the plasma).

Presently, Fokker-Planck solvers have not been incorporated into 2D or 3D radiative hydrodynamic codes for a complete nonlocal plasma simulation predictive capability. More computationally efficient reduced models that can be embedded into fluid codes and preserve nonlocality of electron transport have been developed. We have used one of such nonlinear models [28], that in the limit of small perturbations reproduces the exact linear nonlocal hydrodynamics [12]. The experimental temperature profile, $T_e(x)$ at the peak of the heating cycle is used as initial condition for the hot spot relaxation (HSR) problem:

$$\frac{\partial T_e}{\partial t} - \frac{2}{3n_e}\frac{\partial q(x,t)}{\partial x} = 0, \tag{2}$$

where the electron heat flux $q(x,t)$ is defined as follows,

$$q(x) = \int_{-\infty}^{\infty} q_{SH}(x')G(x,x')dx' , \tag{3}$$

with $q_{SH}(x) = -\kappa_0 \partial T_e/\partial t$ the Spitzer-Härm heat flux,

$$\kappa_0 = \frac{128}{3\pi}\gamma_\kappa n_e v_{Te}\lambda_{ei}\,, \quad \gamma_\kappa = \frac{0.24+Z}{4.2+Z} \qquad (4)$$

where the electron ion mean free path is $\lambda_{ei}(T_e) = 3T_e^2/4\sqrt{2\pi}Zn_e e^4\Lambda$ (Λ is the Coulomb logarithm). The essential details of the transport are included in the kernel $G(x,x')$. Spitzer-Härm transport is reproduced by setting $G(x,x') = \delta(x-x')$ in Eq. (3). As a nonlocal transport model we have used

$$G(x,x') = \frac{\xi(\eta(x-x',x'))}{\pi a \lambda_e(x')}\,, \quad \xi(\eta) = \int_0^\infty \frac{dp \cos \eta p}{1+p^{0.9}}\,, \qquad (5)$$

where $\eta = \mid x - x' \mid / a\lambda_e(x')$. This form of the nonlocal kernel is a generalization of the linear nonlocal theory results for the thermal transport conductivity [12] in the Fourier space ($k \to x - x'$):

$$\kappa(k) = \frac{\kappa_0}{1+(ak\lambda_e)^{0.9}}\,, \quad \lambda_e = \sqrt{Z}\lambda_{ei}\,, \quad k\lambda_{ei} \lesssim 1\,, \qquad (6)$$

where $a = 10(Z+5)/(Z+12)$. However, we also account for the local variations of $n_e(x')$, $T_e(x')$ in λ_e. This approach indeed shows good agreement with the measured temperature profiles in Figure 3.

In summary, we have presented the first measurement of a nonlocal heat wave propagation in a laser produced plasma. Our temperature and density profiles have been directly applied to test theoretical transport models. Calculations based on classical local hydrodynamics, Fokker-Planck codes and semi-analytical solutions of the nonlocal transport equations have been compared showing the importance of kinetic nonlocal effects in electron transport, and finding good agreement with the latter two models. These results will be important to understand the energy deposition mechanisms in laser produced plasmas, in particular for the modeling of hohlraum targets for ICF research.

This work was performed under the auspices of the U.S. Department of Energy by the University of California Lawrence Livermore National Laboratory under Contract No. W-7405-ENG-48. The SPARK code was developed at the University of Rochester's Laboratory for Laser Energetics supported by the US DOE under contract No. DE-FC03-92SF19460.

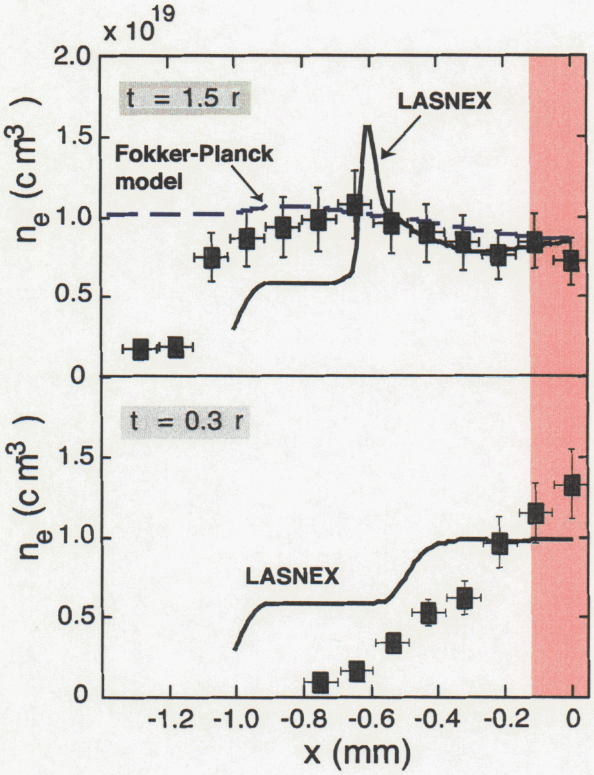

FIG. 4: Electron density profiles at $t = 0.3$ ns and $t = 1.5$ ns. The shaded area corresponds to the heated area by the 1ω driver beam.

---

[*] Lawrence Livermore National Laboratory, University of California, P.O. Box 808, CA 94551

[†] Department of Physics, University of Alberta, Edmonton, Alberta, Canada T6G2J1

[‡] P. N. Lebedev Physics Institute, Russian Academy of Sciences, Moscow 117924, Russia

[1] J. D. Lindl, *Inertial Confinement Fusion* (Springer-Verlag, New York, 1998).
[2] D. S. Montgomery *et al.*, Phys. Rev. Lett. **73**, 2055 (1994).
[3] C. A. Back *et al.*, Phys. Rev. Lett. **77**, 4350 (1996).
[4] S. H. Glenzer *et al.*, Phys. Plasmas **6**, 2117 (1999).
[5] D. R. Gray and J. D. Kilkenny, Plasma Phys. **22**, 81 (1980).
[6] A. R. Bell *et al.*, Phys. Rev. Lett. **46**, 243 (1981).
[7] J.-P. Matte and J. Virmont, Phys. Rev. Lett. **49**, 1936 (1982).
[8] R. J. Mason, Phys. Rev. Lett. **47**, 652 (1981).
[9] J. F. Luciani, P. Mora, and J. Virmont, Phys. Rev. Lett. **51**, 1664 (1983).
[10] J. R. Albritton *et al.*, Phys. Rev. Lett. **57**, 1887 (1986).
[11] E. M. Epperlein and R. W. Short, Phys. Fluids B **3**, 3092 (1991).
[12] V. Y. Bychenkov *et al.*, Phys. Rev. Lett. **75**, 4405 (1995).
[13] A. V. Brantov *et al.*, Phys. Plasmas **5**, 2742 (1998).
[14] L. Spitzer and R. Härm, Phys. Rev. **89**, 977 (1953).
[15] A. V. Brantov, V. Y. Bychenkov, and W. Rozmus, Phys. Plasmas **8**, 3558 (2001).
[16] S. H. Glenzer *et al.*, Phys. Rev. Lett. **88**, 235002 (2002).
[17] F. Aminaroff *et al.*, Phys. Rev. E **61**, 1949 (2000).
[18] A. Gawron *et al.*, Phys. Rev. A **38**, 4737 (1988).
[19] H. J. Kunze, in *Plasma Diagnostics*, edited by Lochte-Holgreven (John Wiley & Sons, New York, 1995).
[20] D. E. Evans and J. Katzenstein, Rep. Prog. Phys. **32**, 207 (1969).
[21] D. Salzmann, *Atomic Processes in Hot Plasmas* (Oxford University Press, Oxford, UK, 1998).

[22] V. Y. Bychenkov *et al.*, Phys. Plasmas **7**, 1511 (2000).
[23] V. Malka *et al.*, Phys. Rev. Lett. **90**, 075002 (2003).
[24] G. B. Zimmerman and W. L. Kruer, Comm. Plasma Phys. **2**, 51 (1975).
[25] R. C. Malone *et al.*, Phys. Rev. Lett. **34**, 721 (1975).
[26] E. M. Epperlein, G. J. Rickard, and A. R. Bell, Comput. Phys. Commun. **52**, 7 (1988).
[27] R. P. J. Town, A. R. Bell, and S. J. Rose, Phys. Rev. E **50**, 1413 (1994).
[28] O. V. Batishchev *et al.*, Phys. Plasmas **9**, 2302 (2002).